



High-resolution SOFIA/EXES Spectroscopy of SO₂ Gas in the Massive Young Stellar Object MonR2 IRS3: Implications for the Sulfur Budget

Ryan Dungee¹, Adwin Boogert¹, Curtis N. DeWitt², Edward Montiel³, Matthew J. Richter³, Andrew G. Barr⁴, Geoffrey A. Blake^{5,6}, Steven B. Charnley⁷, Nick Indriolo⁸, Agata Karska⁹, David A. Neufeld¹⁰, Rachel L. Smith^{11,12}, and Alexander G. G. M. Tielens⁴

¹ Institute for Astronomy, University of Hawaii, 2680 Woodlawn Drive, Honolulu, HI 96822, USA; rdungee@hawaii.edu

² USRA, SOFIA, NASA Ames Research Center, MS 232-11, Moffett Field, CA 94035, USA

³ Department of Physics, University of California, Davis, 1 Shields Avenue, Davis, CA 95616, USA

⁴ Leiden Observatory, Leiden University, P.O. Box 9513, 2300 RA Leiden, The Netherlands

⁵ Division of Geological and Planetary Sciences, MC 150-21, California Institute of Technology, 1200 E. California Boulevard, Pasadena, CA 91125, USA

⁶ Division of Chemistry and Chemical Engineering, California Institute of Technology, 1200 E. California Boulevard, Pasadena, CA 91125, USA

⁷ NASA Goddard Space Flight Center, 8800 Greenbelt Road, MD 20771, USA

⁸ Space Telescope Science Institute, 3700 San Martin Drive, Baltimore, MD 21218, USA

⁹ Centre for Astronomy, Faculty of Physics, Astronomy and Informatics, Nicolaus Copernicus University, Grudziadzka 5, 87-100 Torun, Poland

¹⁰ Department of Physics and Astronomy, Johns Hopkins University, 3400 N. Charles Street, Baltimore, MD 21218, USA

¹¹ North Carolina Museum of Natural Sciences, 121 West Jones Street, Raleigh, NC 27603, USA

¹² Department of Physics and Astronomy, Appalachian State University, 525 Rivers Street, Boone, NC 28608-2106, USA

Received 2018 September 4; revised 2018 October 17; accepted 2018 October 26; published 2018 November 16

Abstract

Sulfur has been observed to be severely depleted in dense clouds leading to uncertainty in the molecules that contain it and the chemistry behind their evolution. Here, we aim to shed light on the sulfur chemistry in young stellar objects (YSOs) by using high-resolution infrared spectroscopy of absorption by the ν_3 rovibrational band of SO₂ obtained with the Echelon-Cross-Echelle Spectrograph on the Stratospheric Observatory for Infrared Astronomy. Using local thermodynamic equilibrium models we derive physical parameters for the SO₂ gas in the massive YSO MonR2 IRS3. This yields a SO₂/H abundance lower limit of $5.6 \pm 0.5 \times 10^{-7}$, or $>4\%$ of the cosmic sulfur budget, and an intrinsic line width (Doppler parameter) of $b < 3.20 \text{ km s}^{-1}$. The small line widths and high temperature ($T_{\text{ex}} = 234 \pm 15 \text{ K}$) locate the gas in a relatively quiescent region near the YSO, presumably in the hot core where ices have evaporated. This sublimation unlocks a volatile sulfur reservoir (e.g., sulfur allotropes as detected abundantly in comet 67P/Churyumov–Gerasimenko), which is followed by SO₂ formation by warm, dense gas-phase chemistry. The narrowness of the lines makes formation of SO₂ from sulfur sputtered off grains in shocks less likely toward MonR2 IRS3.

Key words: astrochemistry – infrared: ISM – ISM: individual objects (MonR2 IRS3) – ISM: molecules

1. Introduction

As a dense cloud begins to collapse into a star it reaches densities high enough (i.e., $n \gtrsim 10^3 \text{ cm}^{-3}$) to enable the formation of a variety of molecules, particularly in the icy mantles that form around dust grains. Understanding the chemistry from which these molecules originate can provide insight into the processes by which stars and planets form. Various molecules have been proposed as tracers of evolution in protostellar environments (Hatchell et al. 1998; Buckle & Fuller 2003). Furthermore, the molecules produced inside these dense clouds will become components of the comets and planetesimals that are created and thus enrich the planetary system that forms (Visser et al. 2009).

Sulfur is the tenth most abundant element in the universe and has a very rich chemistry, meaning that it is well suited for understanding these processes (Charnley 1997; Hatchell et al. 1998; Buckle & Fuller 2003). In the solar system, sulfur is well studied in cometary bodies (Bockelée-Morvan et al. 2000; Calmonte et al. 2016) allowing us to use sulfur-bearing molecules to study the link between the dense cloud, protostellar envelope, and primitive solar system objects. Moreover, there is evidence to suggest that sulfur is necessary for life as we know it (Chen et al. 2015).

However, sulfur has long been measured to be significantly depleted in dense clouds relative to abundances measured in

diffuse clouds, H II regions, and the solar photosphere (Tieftrunk et al. 1994). While this depletion is true for several elements key to astrochemistry, it is especially true for sulfur that has been observed to have abundances in dense clouds as low as 5% of the measured cosmic abundance (Boogert et al. 2015 and references therein). This depletion stands in spite of the variety of sulfur-bearing species that have already been observed in the gas phase in dense clouds and star-forming regions by their rotational line emission (e.g., Blake et al. 1994; Hatchell et al. 1998; van der Tak et al. 2003; Crockett et al. 2014; Drozdovskaya et al. 2018). Ice-phase observations have proven particularly difficult with only the detection of OCS (Palumbo et al. 1997) and, tentatively, SO₂ (Boogert et al. 1997; Zasowski et al. 2009). Thus, the majority of the sulfur is either contained in refractory material (e.g., FeS; Keller et al. 2002) or in alternate volatile molecules.

Here, we use high-resolution ($R = \lambda/\Delta\lambda = 55,000$) mid-infrared spectra to further study gas-phase SO₂ molecules. Mid-infrared wavelengths enable studying the SO₂ nearest the hot core of MonR2 IRS3 through its absorption of the warm dust continuum. Previously, the *Infrared Space Observatory* (ISO) measured the absorption of SO₂ in this and several other massive young stellar objects (YSOs; Keane et al. 2001). However, it was impossible to resolve individual lines at the resolution ($R = 2000$) of ISO. With the high-resolution

Table 1
Observation Log

Target	UTC Start Time (YYYY mm dd hh:mm)	Altitude (start/end)	Latitude (start/end)	Longitude (start/end)	Elevation (start/end)
MonR2 IRS3	2017 Jan 24 03:06	41000/42000 ft	48°1/44°6 N	98°7/113°8 W	33°/37°
Sirius	2017 Jan 24 04:38	43000 ft	44°3/41°5 N	115°4/124°4 W	26°/29°

Echelon-Cross-Echelle Spectrograph (EXES; Richter et al. 2010) on the Stratospheric Observatory for Infrared Astronomy (SOFIA; Temi et al. 2014) we can now measure the line width and investigate the location and chemical origin of this gas. For example, lines that are tens of km s^{-1} wide would indicate shocks capable of sputtering sulfur off refractory grains (May et al. 2000), while narrower lines in a warm gas would be a signature of ice sublimation by stellar heat.

2. Observations and Data Reduction

For the SO_2 observations (Table 1), EXES was operated in the high-resolution configuration with a slit width of $3''/2$ providing for a spectral resolution (R) of $55,000 \pm 1100$ (1σ). The resolution is assumed to be constant as a function of wavelength (λ) for a given slit width and is extrapolated from C_2H_2 gas cell absorption measurements at $\lambda = 7.30 \mu\text{m}$. The medium-resolution cross disperser was used with a slit length of $7''/7$. The spectra collected span from 7.23 to 7.30 and 7.31 to $7.38 \mu\text{m}$, covering the ν_3 rovibrational band of SO_2 .

Data were reduced using the EXES instrument pipeline (Redux; Clarke et al. 2015) up until the order-merging step at which point our custom software was used. First, we applied extra cuts to the data where the pipeline’s reported signal-to-noise ratio (S/N) began decreasing ($S/N < 6.0$) at the edges of the instrument’s blaze function. Next, we applied telluric absorption corrections using atmospheric spectra generated by the Planetary Spectrum Generator (PSG; Villanueva et al. 2018). The telluric lines were also used to improve the wavenumber calibration of the data to an accuracy of 0.005 cm^{-1} (1 km s^{-1}), since the absorption features have wavenumbers known to high precision in the high-resolution transmission molecular absorption database (HITRAN; Gordon et al. 2017). Subsequently, we divided our data by spectra of the standard star, Sirius, observed on the same flight to correct for fringes in the data. Spectral orders were then stitched together by a combined process of linear interpolation and weighted averaging of the overlapping sections. Finally, we normalized the spectra to the background continuum defined by a low amplitude, slowly varying sin function, fit to regions of the data least affected by absorption lines. A systematic continuum uncertainty of $\sim 3\%$ is folded into the absorption line depth uncertainties.

MonR2 IRS3 was also observed with the NIRSPEC spectrometer (McLean et al. 1998) at the Keck II telescope in the atmospheric M band at $R = 25,000$, as part of a survey exploring CO isotopologue abundances in a range of YSOs (R. L. Smith et al. 2018, in preparation). Here, the data for MonR2 IRS3 were used to measure gas-phase CO column densities and line profiles to determine SO_2/CO and, subsequently, SO_2/H abundance ratios (Section 3.3). For further information on these observations and their reduction see Smith et al. (2016).

3. Modeling Absorption

The observed spectra show many absorption features (Figure 1). We used local thermodynamic equilibrium (LTE) models to generate model absorption spectra from which we derive physical parameters.

3.1. Generating Model Spectra

The models assume SO_2 and ^{13}CO are present in a uniform slab perpendicular to and covering the line of sight. Given a column density (N , cm^{-2}), an excitation temperature (T_{ex} , K), an intrinsic line width (or Doppler parameter, b , km s^{-1} , related to the FWHM by $\text{FWHM} = 2b\sqrt{\ln 2}$), and a Gaussian instrumental line spread function, the LTE model generates an absorption spectrum.

The molecular line parameters (Einstein A coefficient, partition function table, and quantum numbers) were retrieved from the HITRAN database. These parameters were used to calculate the population in each energy level for a gas with temperature T_{ex} and total column N following the standard Boltzmann equation. Subsequently, line equivalent widths were calculated and then converted to line profiles of width b at infinite resolution. Each line has a Voigt profile that is then convolved with a Gaussian profile to the instrumental resolution and used to compute a continuum normalized intensity.

3.2. Fitting to the Data

The LTE model was fit across the whole spectrum simultaneously and the best fit was found by using a χ^2 value as our maximum likelihood estimator. To obtain the uncertainties, we used a Markov Chain Monte Carlo (MCMC) sampling to determine the posterior distributions of our model parameters. From these posterior distributions we obtained the 68% credibility interval. To do the sampling we used the open source Python package `emcee` (Foreman-Mackey et al. 2013). Figure 1 shows selected subsets of our best fits plotted over the data. The Doppler shift of the target is not a parameter we fit for; instead, we adopted a value based off the V_{LSR} of 10 km s^{-1} measured in previous submillimeter studies of MonR2 IRS3 (van der Tak et al. 2003) and in good agreement with our SO_2 and ^{13}CO observations (Figure 2).

Concurring with previous studies (Giannakopoulou et al. 1997; Smith et al. 2016), we fit two temperature components to the observations for both SO_2 and ^{13}CO . The priors common to all of our fits were the restrictions that $T_{\text{ex}} > 1$, $N > 0.0$, and $b > 0.0$. We also folded an uncertainty on spectral resolution into our determination of b , the prior for this was a Gaussian distribution. For EXES the peak probability occurred at $R = 55,000$ with a standard deviation of 1100, and for NIRSPEC the peak probability occurred at $R = 25,000$ and was uncertain to 10% at the 3σ level.

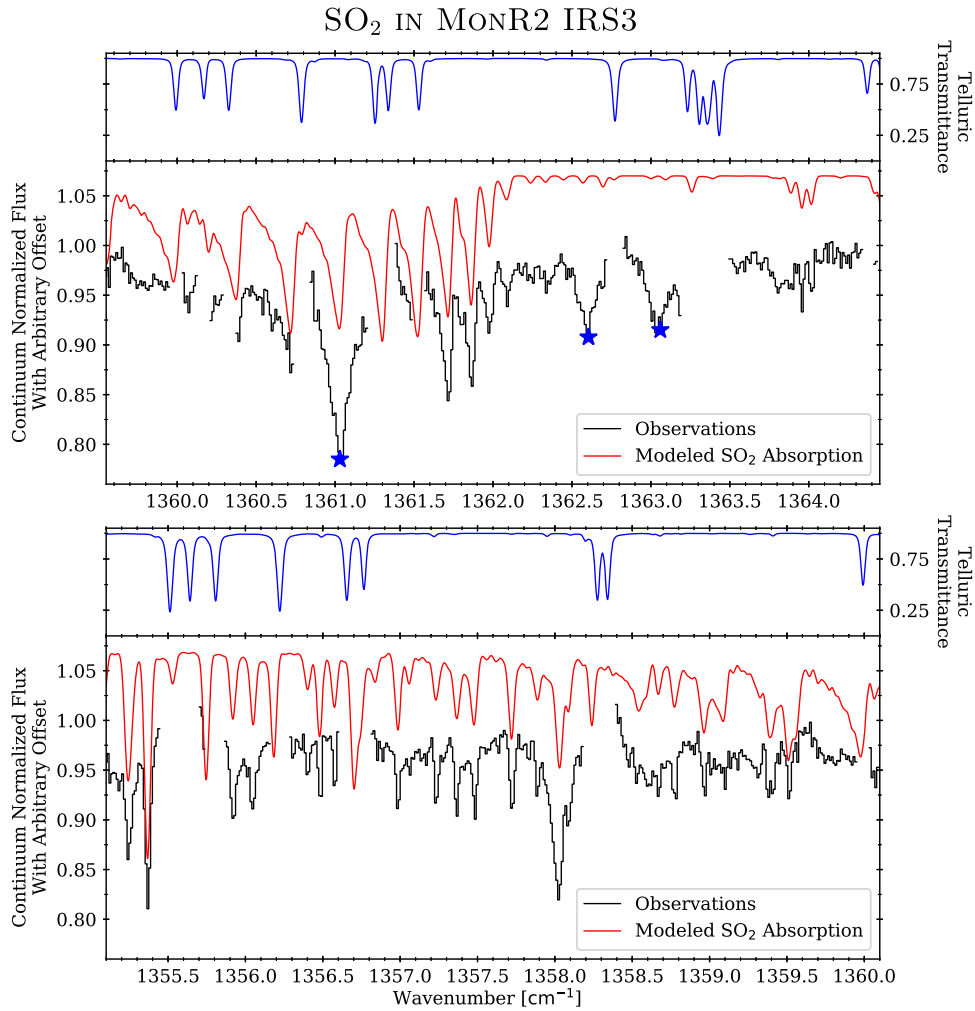


Figure 1. Subsets of the observed spectra of MonR2 IRS3 with the best-fit local thermodynamic equilibrium (LTE) model plotted in red; telluric transmission is plotted in blue. Data are plotted in the rest frame of MonR2 IRS3 ($V_{\text{LSR}} = 10 \text{ km s}^{-1}$). For the best-fit parameters and their definitions, see Section 3.1. We use the upper limit Doppler parameter (3.20 km s^{-1}) in generating the plotted model. Gaps in the data represent regions where the telluric transmission drops below 80%. Blue stars denote absorption features due H_2O in the target.

Fitting for the warm SO_2 alone, we found a T_{ex} of $234 \pm 15 \text{ K}$, an N of $4.95^{+0.29}_{-0.30} \times 10^{16} \text{ cm}^{-2}$, and an upper limit of $b < 3.20 \text{ km s}^{-1}$. The cold component was much less well determined, and so we only quote upper limits at the 95% confidence level: $T_{\text{ex}} < 88 \text{ K}$ and $N < 1.3 \times 10^{14} \text{ cm}^{-2}$, assuming the same upper limit on the Doppler parameter.

For the ^{13}CO we first measured the Doppler parameter by stacking the absorption features in our spectrum and measuring the line width assuming a Gaussian line profile and R of 25,000 (this approach is not possible for the crowded SO_2 spectrum). This yielded b values of 7.4 ± 2.2 and $5.3 \pm 2.1 \text{ km s}^{-1}$ for the warm and cold ^{13}CO components, respectively. These values were then used as additional priors. The other key difference from our SO_2 analysis was that we fit the warm ^{13}CO to the high- J level transitions, where it is the only contributor, before fitting a cold component on top of the now determined warm component in the low- J level transitions. A single temperature component was unable to produce deep absorption features in both low- J level transitions and high- J level transitions. This yielded a best fit for the warm ^{13}CO component of $T_{\text{ex}} = 240 \pm 25 \text{ K}$ and $N = 1.1 \pm 0.2 \times 10^{17} \text{ cm}^{-2}$, and a cold component with $T_{\text{ex}} = 10 \pm 7 \text{ K}$ and $N = 3.7^{+0.6}_{-1.0} \times 10^{16} \text{ cm}^{-2}$. These values are consistent with

those found by a curve of growth analysis (Smith et al. 2016, R. L. Smith et al. 2018, in preparation).

3.3. Abundances

Since the measured line width for the warm ^{13}CO gas ($7.4 \pm 2.2 \text{ km s}^{-1}$) is broader than that of the SO_2 gas ($< 3.20 \text{ km s}^{-1}$), we are possibly including additional gas not associated with the reservoir of SO_2 we observed. Assuming a typical $^{12}\text{CO}/^{13}\text{CO} = 80$ and $\text{H}_2/^{12}\text{CO} = 5000$ (Lacy et al. 1994), we derive a lower limit on the abundance of SO_2 relative to N_{H} ($=N(\text{H}) + 2N(\text{H}_2)$) of $(5.6 \pm 0.5) \times 10^{-7}$ for the warm SO_2 . Comparing this lower limit to the cosmic sulfur abundance ($\text{S}/\text{H} = 1.3 \times 10^{-5}$; Asplund et al. 2009) shows that this SO_2 gas accounts for $>4\%$ of the sulfur budget. We place an upper limit on the cold SO_2 abundance of 4.4×10^{-9} by using a cold ^{12}CO gas column of $N = 80 \times 3.7 \times 10^{16} = 3.0 \times 10^{18} \text{ cm}^{-2}$. Frozen CO contributes little. Using data from Gibb et al. (2004) we derived a ^{12}CO ice column upper limit of $0.5 \times 10^{17} \text{ cm}^{-2}$.

We also calculate an abundance relative to H_2O , allowing for direct comparison with cometary results. Boonman et al. (2003) reported a column density $N_{\text{H}_2\text{O}} = 5 \pm 2 \times 10^{17} \text{ cm}^{-2}$ with $250^{+200}_{-100} \text{ K}$. This yields a warm abundance, $\text{SO}_2/\text{H}_2\text{O}$, of

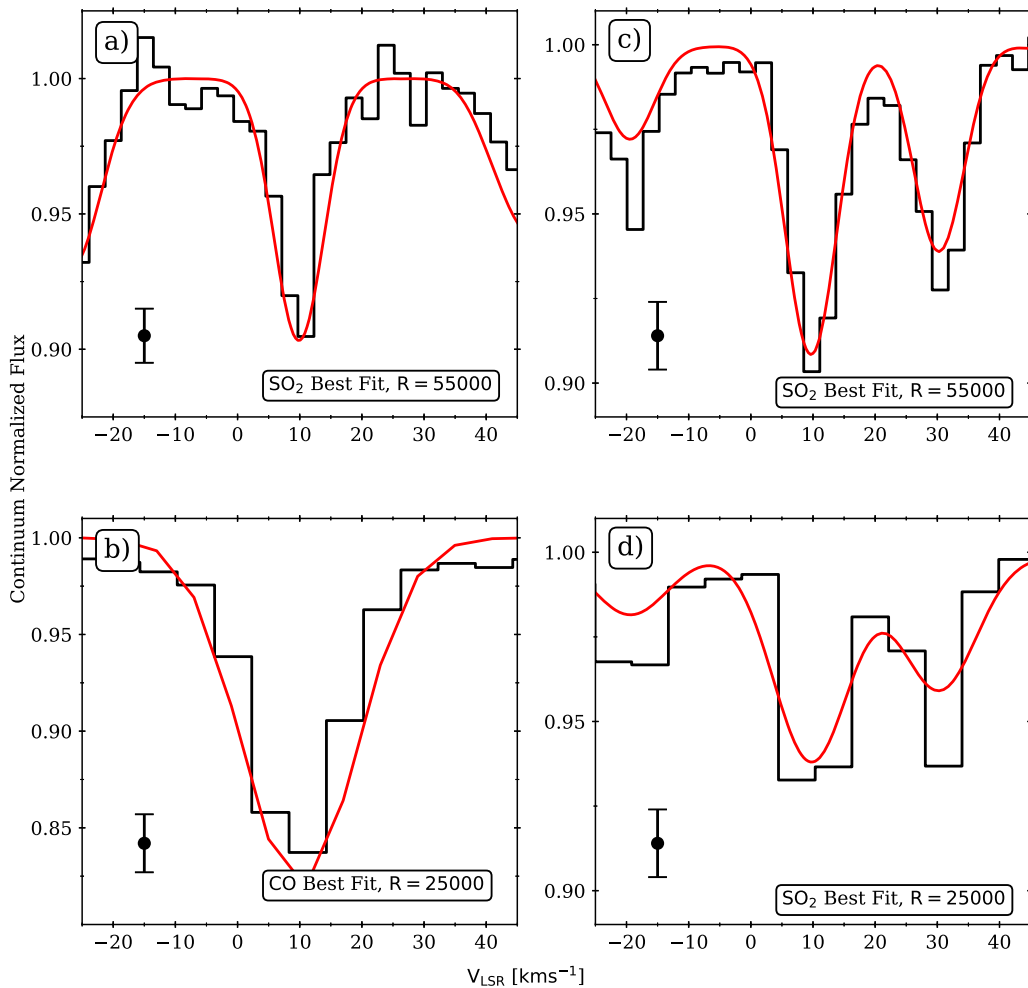


Figure 2. Isolated absorption features from each of our data sets showing line width comparisons. The best-fit model is plotted in red. Note that the $b = 3.20 \text{ km s}^{-1}$ used for SO₂ here is an upper limit for the intrinsic line width. For the best-fit parameters and their definitions, see Section 3.1. Panels (a) and (b) are isolated absorption features from the SO₂ and ¹³CO spectra, respectively. Panels (c) and (d) are of the same SO₂ absorption feature, one convolved to the same resolution as our ¹³CO data. The point with error bars represents the typical uncertainty for the observed spectra in that panel.

$>10 \pm 3\%$. Lacking measurements of the foreground H₂O, we could not do the same for our cold SO₂ measurements. All abundances are summarized in Table 2.

3.4. Comparison with Previous Work

Millimeter-wave observations of MonR2 IRS3 have measured the SO₂ column density at beam sizes of $\sim 15''$, probing the cool envelope (van der Tak et al. 2003). The column density of $1.5 \pm 0.3 \times 10^{14} \text{ cm}^{-2}$ is consistent with our cold SO₂ component's upper bound of $1.3 \times 10^{14} \text{ cm}^{-2}$. Additionally, our measured warm SO₂ component is consistent with infrared measurements by Keane et al. (2001), who reported $T_{\text{ex}} = 225^{+50}_{-70}$ and $N = 4.0 \pm 0.8 \times 10^{16} \text{ cm}^{-2}$ using an adopted b of 3 km s^{-1} .

4. Discussion

The abundance of warm SO₂ gas is over two orders of magnitude higher than the cold gas, suggesting a sulfur reservoir that is unlocked after heating. The small line widths ($b < 3.20 \text{ km s}^{-1}$) likely imply a yet unobserved precursor in the ice, rather than in the refractory materials. Moreover, the warm gas-phase SO₂/H₂O ratio of $10 \pm 3\%$ is at least a factor 10 larger than that observed in the foreground ice toward this target

(Table 2). All of this hints at an efficient gas-phase process that converts the sublimated sulfur-bearing ice molecules into SO₂.

4.1. SO₂ Formation

Shocks have previously been observed to lead to substantial enhancements in SO₂ abundances (Pineau des Forets et al. 1993; Bachiller & Pérez Gutiérrez 1997; Podio et al. 2015). The extreme temperatures enable a variety of gas-phase reactions of pre-shock gas or sublimated ices that enhance the formation of SO₂. Indeed, shock chemistry models successfully replicated the measured abundance of gas-phase SO₂ toward the Orion Plateau, which shows very broad lines indicative of shocks generated by Orion IRc 2 outflows ($b \gtrsim 12\text{--}15 \text{ km s}^{-1}$; Blake et al. 1987). Also, shocks of tens of km s^{-1} can shatter or sputter dust grains (May et al. 2000), possibly leading to the release of more sulfur and subsequent SO₂ formation. However, the SO₂ lines toward MonR2 IRS3 are substantially narrower ($b < 3.20 \text{ km s}^{-1}$; Figure 2) than those in the Orion Plateau. Our results are therefore more consistent with release from the ices due to radiative heating (or perhaps mild shocks) rather than from refractory grains in strong shocks. Also, the SO₂/H abundance derived for MonR2 IRS3 (0.6×10^{-6}) is somewhat higher than that measured in

Table 2
Abundances of Sulfur-bearing Molecules toward MonR2 IRS3 and Comet 67/P

Species	Hot Core ^a		Foreground Gas ^b	Foreground Ice		Comet 67/P's Coma
	X_{H} 10^{-7}	$X_{\text{H}_2\text{O}}$ %		X_{H} ^c 10^{-7}	$X_{\text{H}_2\text{O}}$ ^d %	
SO ₂	$>5.6 \pm 0.5$	10 ± 3	<0.044	<5.7 (1)	<0.6 (1)	0.127 ± 0.003 (4)
H ₂ S	<2.8 (2)	<1.1 (2)	1.10 ± 0.05 (4)
OCS	<0.18 (3)	<0.07 (3)	0.041 ± 0.001 (4)
S ₂	0.197 ± 0.003 (4)

Notes. Sources: (1) derived from data in Gibb et al. (2004), (2) Smith (1991), (3) Palumbo et al. (1997), (4) Calmonte et al. (2016).

^a Calculated from an SO₂ column of $4.95 \times 10^{16} \text{ cm}^{-2}$, and a derived hydrogen column of $8.8 \times 10^{22} \text{ cm}^{-2}$ or an H₂O column of $5 \times 10^{17} \text{ cm}^{-2}$ (Section 3.3).

^b Calculated from an SO₂ column of $1.3 \times 10^{14} \text{ cm}^{-2}$, and a hydrogen column of $3.0 \times 10^{22} \text{ cm}^{-2}$ (Section 3.3).

^c Relative to a hydrogen column of $3.0 \times 10^{22} \text{ cm}^{-2}$ derived from our cold ¹³CO gas column (Section 3.3).

^d Relative to an ice column $N_{\text{H}_2\text{O}} = 1.9 \times 10^{18} \text{ cm}^{-2}$ (Gibb et al. 2004).

Orion IRc 2 (0.2×10^{-6} ; Blake et al. 1987) and consistent with the range reported for the outflow target HH 212 ($(0.4\text{--}1.2) \times 10^{-6}$; Podio et al. 2015). The formation of SO₂ in hot cores is thus at least as efficient as in shocks and, importantly, sputtering of sulfur off of grains does not seem to be a required process.

This process, for the first time observed in a massive hot core, might also be important in lower-mass YSOs. The strong enhancement of SO molecules observed in a protoplanetary disk (Booth et al. 2018) might thus relate to ice sublimation rather than grain sputtering in shocks.

4.2. Progenitor Species

There still remains the question of which molecular species lead to the efficient formation of gas-phase SO₂. The large mismatch between ice-phase detections of SO₂ (Boogert et al. 1997; Zasowski et al. 2009) and the warm component we measured indicate that SO₂ cannot be sublimating directly from the ice. Chemical models generally rely on large abundances of sublimated H₂S ice for SO₂ formation (Charnley 1997; Woods et al. 2015). Indeed, measurements by the ROSINA experiment have shown that H₂S is the largest contributor to the sulfur budget in the comet 67P/Churyumov–Gerasimenko (Calmonte et al. 2016). In stark contrast, H₂S ice measurements toward dense clouds and protostellar envelopes yielded upper limits (Smith 1991; Jiménez-Escobar & Muñoz Caro 2011) a factor of two below our gas-phase SO₂ abundance (Table 2), and we thus hesitate to conclude this is the primary source of sulfur that is driven into SO₂ molecules. Instead, we consider the release of sulfur allotropes (e.g., S₂, S₃, S₄) that have been shown to be the second most abundant sulfur carrier in the ices of comet 67P (Calmonte et al. 2016; Drozdovskaya et al. 2018). These allotropes can be broken apart by helium atoms, allowing for gas-phase reactions between OH, O₂, and S that lead to the formation of SO₂ (McElroy et al. 2013).

Chemical models suggest that at temperatures $\gtrsim 230$ K the oxygen is preferentially driven into H₂O (Charnley 1997; Doty et al. 2002; van Dishoeck et al. 2011). The measured SO₂ temperature is comparable to this threshold. This suggests the gas-phase formation of SO₂ in MonR2 IRS3 is suppressed in favor of the production of H₂O, though our results are not inconsistent with sub-230 K temperatures. Alternatively, the SO₂ we observe formed before further heating of the gas, or at larger, cooler radii. High H₂O abundances were measured along this line of sight, though there remains the possibility that these observations probed a

warmer region closer to the hot core than the SO₂ gas we observed. This cannot be excluded following observations by Boonman et al. (2003), who measured a temperature of 250_{-100}^{+200} K. A high spectral resolution analysis by N. Indriolo et al. (2018, in preparation) is expected to shed more light on this possibility.

4.3. Critical Density

The basis for the LTE assumption is that collisional excitations at least match the rate of radiative de-excitations. The minimum density at which this occurs is called the critical density, and values for SO₂ are of order 10^6 cm^{-3} to 10^7 cm^{-3} (Wakelam et al. 2004; Williams & Viti 2014). Using a modeled temperature profile for a hot core from van der Tak et al. (1999) and the radial density profile of MonR2 IRS3 reported by van der Tak et al. (2000), we find that SO₂ with a temperature of 230 K is expected to reside at a radius of ~ 500 au with a particle density of $n = 6 \times 10^6 \text{ cm}^{-3}$, comparable to the SO₂ critical densities. Also, the critical density of ¹³CO is over an order of magnitude smaller than that of SO₂, and thus ¹³CO is most likely in LTE. The similarity of the excitation temperatures of these molecules thus further indicates that the SO₂ transitions are thermalized.

5. Conclusions

We have measured a warm SO₂ gas with temperature 234 ± 15 K and an abundance with respect to hydrogen $>5.6 \pm 0.5 \times 10^{-7}$ with narrow line widths ($b < 3.20 \text{ km s}^{-1}$) in the massive YSO MonR2 IRS3. These infrared absorption values confirm the existence of a large reservoir of sulfur that has been unobserved in past submillimeter observations. Moreover, this warm SO₂ contributes $>4\%$ of the sulfur budget in our target. The small line widths are inconsistent with SO₂ formation from sulfur sputtered off refractory grains in strong shocks. Thus, we conclude the abundant SO₂ gas likely originates from sublimated ices in the hot core close to the massive YSO. Past H₂S and SO₂ ice observations indicate that they are unlikely precursors to this gas, leading us to conclude there is a large reservoir of sulfuretted molecules in the ice that has yet to be observed. Based on comet 67P measurements these might be sulfur allotropes. Future observations of sulfur-containing ices in samples of dense clouds and YSOs by the planned *James Webb Space Telescope* should help us to confirm this hypothesis. However, the direct detection of sulfur allotropes is unlikely, considering their infrared absorption bands are weak and broad ($17\text{--}50 \mu\text{m}$; e.g., Mahjoub et al. 2017). High

spectral resolution observations of gas-phase SO₂ with EXES on SOFIA toward a larger sample of YSOs are also needed to further distinguish between quiescent hot core and shocked environments. Additionally, higher-resolution spectra for ¹³CO obtained by an instrument such as iSHELL (Rayner et al. 2016) will allow for better characterization of the dynamical components from the ¹³CO line profile and SO₂ abundances in each component.

Based in part on observations made with the NASA/DLR Stratospheric Observatory for Infrared Astronomy (SOFIA). SOFIA is jointly operated by the Universities Space Research Association, Inc. (USRA), under NASA contract NNA17BF53C, and the Deutsches SOFIA Institut (DSI) under DLR contract 50 OK 0901 to the University of Stuttgart. Financial support for this work was provided by NASA through award No. SOF 04-153 issued by USRA.

Some of the data presented herein were obtained at the W. M. Keck Observatory, which is operated as a scientific partnership among the California Institute of Technology, the University of California and the National Aeronautics and Space Administration. The Observatory was made possible by the generous financial support of the W. M. Keck Foundation. The authors wish to recognize and acknowledge the very significant cultural role and reverence that the summit of Maunakea has always had within the indigenous Hawaiian community. We are most fortunate to have the opportunity to conduct observations from this mountain.




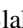



A.K. acknowledges support from the Polish National Science Center grant 2016/21/D/ST9/01098.

R.L.S. gratefully acknowledges support under NASA Emerging Worlds grant NNX17AE34G.

Facility: SOFIA.

Software: Redux (Clarke et al. 2015), emcee (Foreman-Mackey et al. 2013), PSG (Villanueva et al. 2018).

ORCID iDs

Ryan Dungee  <https://orcid.org/0000-0001-6669-0217>
 Adwin Boogert  <https://orcid.org/0000-0001-9344-0096>
 Matthew J. Richter  <https://orcid.org/0000-0002-8594-2122>
 Andrew G. Barr  <https://orcid.org/0000-0003-4909-2770>
 Geoffrey A. Blake  <https://orcid.org/0000-0003-0787-1610>
 Nick Indriolo  <https://orcid.org/0000-0001-8533-6440>
 Agata Karska  <https://orcid.org/0000-0001-8913-925X>
 David A. Neufeld  <https://orcid.org/0000-0001-8341-1646>

References

Asplund, M., Grevesse, N., Sauval, A. J., et al. 2009, *ARA&A*, 47, 481
 Bachiller, R., & Pérez Gutiérrez, M. 1997, *ApJL*, 487, L93
 Blake, G. A., Sutton, E. C., Masson, C. R., et al. 1987, *ApJ*, 315, 621

Blake, G. A., van Dishoeck, E. F., Jansen, D. J., et al. 1994, *ApJ*, 428, 680
 Bockelée-Morvan, D., Lis, D. C., Wink, J. E., et al. 2000, *A&A*, 353, 1101
 Boogert, A. C. A., Gerakines, P. A., & Whittet, D. C. B. 2015, *ARA&A*, 53, 541
 Boogert, A. C. A., Schutte, W. A., Helmich, F. P., et al. 1997, *A&A*, 317, 929
 Boonman, A. M. S., Doty, S. D., van Dishoeck, E. F., et al. 2003, *A&A*, 406, 937
 Booth, A. S., Walsh, C., Kama, M., et al. 2018, *A&A*, 611, A16
 Buckle, J. V., & Fuller, G. A. 2003, in ASP Conf. Ser. 287, Galactic Star Formation Across the Stellar Mass Spectrum, ed. J. M. De Buizer & N. S. van der Blik (San Francisco, CA: ASP), 146
 Calmonte, U., Altwegg, K., Balsiger, H., et al. 2016, *MNRAS*, 462, S253
 Charney, S. B. 1997, *ApJ*, 481, 396
 Chen, Y.-J., Juang, K.-J., Nuevo, M., et al. 2015, *ApJ*, 798, 80
 Clarke, M., Vacca, W. D., Shuping, R. Y., et al. 2015, in ASP Conf. Proc. Astronomical Data Analysis Software and Systems XXIV, ed. A. R. Taylor & E. Rosolowsky (San Francisco, CA: ASP), 355
 Crockett, N. R., Bergin, E. A., Neill, J. L., et al. 2014, *ApJ*, 787, 112
 Doty, S. D., van Dishoeck, E. F., van der Tak, F. F. S., et al. 2002, *A&A*, 389, 446
 Drozdovskaya, M. N., van Dishoeck, E. F., Jørgensen, J. K., et al. 2018, *MNRAS*, 476, 4949
 Foreman-Mackey, D., Hogg, D. W., Lang, D., et al. 2013, *PASP*, 125, 306
 Giannakopoulou, J., Mitchell, G. F., Hasegawa, T. I., et al. 1997, *ApJ*, 487, 346
 Gibb, E. L., Whittet, D. C. B., Boogert, A. C. A., et al. 2004, *ApJS*, 151, 35
 Gordon, I. E., Rothman, L. S., Hill, C., et al. 2017, *JQSRT*, 203, 3
 Hatchell, J., Thompson, M. A., Millar, T. J., et al. 1998, *A&A*, 338, 713
 Jiménez-Escobar, A., & Muñoz Caro, G. M. 2011, *A&A*, 536, A91
 Keane, J. V., Boonman, A. M. S., Tielens, A. G. G. M., et al. 2001, *A&A*, 376, L5
 Keller, L. P., Hony, S., Bradley, J. P., et al. 2002, *Natur*, 417, 148
 Lacy, J. H., Knacke, R., Geballe, T. R., et al. 1994, *ApJL*, 428, L69
 Lamberts, T., & Kästner, J. 2017, *JPCA*, 121, 9736
 Mahjoub, A., Poston, M. J., Blacksberg, J., et al. 2017, *ApJ*, 846, 148
 May, P. W., Pineau des Forêts, G., Flower, D. R., et al. 2000, *MNRAS*, 318, 809
 McElroy, D., Walsh, C., Markwick, A. J., et al. 2013, *A&A*, 550, A36
 McLean, I. S., Becklin, E. E., Bendiksen, O., et al. 1998, *Proc. SPIE*, 3354, 566
 Palumbo, M. E., Geballe, T. R., & Tielens, A. G. G. M. 1997, *ApJ*, 479, 839
 Pineau des Forets, G., Roueff, E., Schilke, P., et al. 1993, *MNRAS*, 262, 915
 Podio, L., Codella, C., Gueth, F., et al. 2015, *A&A*, 581, A85
 Rayner, J., Tokunaga, A., Jaffe, D., et al. 2016, *Proc. SPIE*, 9908, 990884
 Richter, M. J., Ennico, K. A., McKelvey, M. E., et al. 2010, *Proc. SPIE*, 7735, 77356Q
 Smith, R. G. 1991, *MNRAS*, 249, 172
 Smith, R. L., Blake, G. A., Boogert, A. C. A., et al. 2016, *LPICo*, 3028, 1903
 Temi, P., Marcum, P. M., Young, E., et al. 2014, *ApJS*, 212, 24
 Tieftrunk, A., Pineau Des Forets, G., Schilke, P., et al. 1994, *A&A*, 289, 579
 van der Tak, F. F. S., Boonman, A. M. S., Braakman, R., et al. 2003, *A&A*, 412, 133
 van der Tak, F. F. S., van Dishoeck, E. F., Evans, N. J., et al. 1999, *ApJ*, 522, 991
 van der Tak, F. F. S., van Dishoeck, E. F., Evans, N. J., et al. 2000, *ApJ*, 537, 283
 van Dishoeck, E. F., Kristensen, L. E., Benz, A. O., et al. 2011, *PASP*, 123, 138
 Villanueva, G. L., Smith, M. D., Protopapa, S., et al. 2018, arXiv:1803.02008
 Visser, R., van Dishoeck, E. F., & Black, J. H. 2009, *A&A*, 503, 323
 Wakelam, V., Castets, A., Ceccarelli, C., et al. 2004, *A&A*, 413, 609
 Williams, D. A., & Viti, S. 2014, *Observational Molecular Astronomy* (Cambridge: Cambridge Univ. Press)
 Woods, P. M., Occhiogrosso, A., Viti, S., et al. 2015, *MNRAS*, 450, 1256
 Zasowski, G., Kemper, F., Watson, D. M., et al. 2009, *ApJ*, 694, 459